A Comparative Computational Analysis of Nozzle Geometry Effects on Jet Mixing and Thermal Plume Decay at High Altitude

Aryan Senthilkumar[1]

Northview High School, Johns Creek, Georgia, 30024, USA

Parthiv Prathapaneni[2*]

California High School, San Ramon, California, 94582, USA

Aahan Kumbham[3*]

Panther Creek High School, Frisco, Texas, 75033, USA

Gutti Yashaswini[4*]

Narayana Junior College Chandapura, Bengaluru, Karnataka, 560099, India

Smaran Sure[5*]

Washington High School, Fremont, California, 94536, USA

Dr. Prashanth Prakash[5*]

Massachusetts Institute of Technology, Cambridge, Massachusetts, 02139 USA

Jet plume mixing significantly influences propulsion performance, thermal signature, and exhaust plume control in aerospace propulsion systems. This study investigates the effect of nozzle exit geometry on plume development by comparing four configurations: a conical baseline nozzle, a convergent–divergent (C–D) nozzle, a lobed mixer nozzle, and an elliptic exit nozzle. Three-dimensional unsteady Reynolds-averaged Navier–Stokes (URANS) simulations were performed in ANSYS Fluent under representative high-altitude conditions corresponding to the International Standard Atmosphere at 11 km. The realizable k–epsilon turbulence model was employed to capture turbulent plume mixing. Flow fields were evaluated using centerline velocity decay, normalized temperature decay, root-mean-square velocity fluctuations, and thrust performance to quantify plume mixing behavior and propulsion tradeoffs. Results show that nozzle geometry strongly alters plume evolution through compressibility effects, vortex-induced entrainment, and geometric axis switching. The convergent–divergent nozzle produced the most rapid momentum dissipation, reaching 50 percent velocity decay at $x/D_e \approx 1.3$ compared with $x/D_e \approx 8.9$ for the conical baseline, while also generating the highest thrust (≈ 4,191 N) due to efficient supersonic expansion. The lobed mixer enhanced plume dilution through counter-rotating vortex pairs while maintaining relatively high thrust (≈ 3,183 N). The elliptic nozzle generated the strongest turbulence levels (URMS ≈ 254 m/s) through axis-switching dynamics but reduced axial thrust relative to the baseline. These results demonstrate that compressibility effects, vortex generation, and geometric asymmetry represent distinct mechanisms for enhancing plume mixing, with the lobed mixer providing the most balanced compromise between plume dilution and propulsion efficiency.

[1]Student, AIAA High School Subcommittee, 1858861
[2]Student, AIAA High School Subcommittee, 1924535
[3]Student, AIAA High School Subcommittee, 1822386
[4]Student, AIAA High School Subcommittee, 1845115
[5]Student, AIAA High School Subcommittee, 1860405
[6]Faculty Advisor, Massachusetts Institute of Technology
*2nd authors contributed equally

I. NOMENCLATURE

a = Elliptic nozzle semi-major axis, m
A_t = Nozzle throat area (C-D nozzle)
D_e = Reference exit diameter, m
D_{in} = Nozzle inlet diameter, m
F = Axial wall force (thrust proxy), N
L = Nozzle length, m
M = Local Mach number, −
Po = Inlet gauge total pressure, Pa
R = Specific gas constant, J/kg·K
T = Static temperature, K
To = Inlet total temperature, K
Tu = Turbulence intensity, −
x = Axial distance from nozzle exit, m
γ = Ratio of specific heats, −
$\Delta F\%$ = Thrust proxy deviation from baseline, %
Ae = Nozzle exit area, m²
b = Elliptic nozzle semi-minor axis, m
De,eff = Effective exit diameter (4-lobe mixer), m
D_t = Nozzle throat diameter (C-D), m
$F_{baseline}$ = Conical nozzle thrust reference, N
L_c = Thermal core length, m
$\dot{m}$ = Mass flow rate, kg/s
P_{op} = Ambient static pressure, Pa
$r½$ = Plume half-width (UDS = 0.05), m
T_{exit} = Centerline temperature at nozzle exit, K
$T\infty$ = Freestream (ambient) temperature, K
RMS = Root Mean Square velocity magnitude, m/s
x/D_e = Normalized axial distance
Θ = Normalized centerline temperature excess, −

II. INTRODUCTION

The infrared signature of high-speed jet exhaust is a critical vulnerability in military aerospace: heat-seeking missile systems exploit the thermal plume of engine exhaust, making rapid plume decay essential for aircraft survivability. In civil aviation, the same mixing processes govern jet noise and contrail formation. In both contexts, nozzle exit geometry is the primary passive lever available for controlling the rate at which the hot exhaust core entrains surrounding ambient air, and a substantial body of literature has established that geometric modifications can achieve mixing enhancements of up to 100% relative to a plain convergent nozzle [1]. Tabbed and lobed mixer geometries suppress IR signatures through counter-rotating streamwise vortex pairs that dramatically increase jet-ambient interfacial area [2,3,5,12]; elliptic exits produce axis-switching and asymmetric entrainment without internal features [6,7,15,16]; and convergent-divergent nozzles introduce shock-cell structures that directly modulate thermal decay [8]. Despite this breadth, most existing studies evaluate a single geometry class at sea-level conditions, leaving systematic multi-geometry comparisons at high-altitude compressible conditions largely unaddressed.

This work provides a controlled, directly comparable CFD dataset spanning four physically distinct mixing mechanisms: shear-layer instability, shock-cell interaction, inviscid vortex generation, and azimuthal axis-switching under identical high-altitude conditions. The results quantify the trade-off between mixing enhancement and thrust penalty for each geometry, with direct implications for infrared signature management in high-altitude aerospace applications.

III. COMPUTATIONAL APPROACH

A. Flow Conditions and Domain

All simulations are performed at 11 km ISA altitude conditions: ambient static pressure P_s = 22,632 Pa, ambient temperature $T\infty$ = 216.65 K, and ambient density $\rho\infty$ = 0.3639 kg/m³. The nozzle inlet is specified as a pressure inlet with gauge total pressure P_0 = 97,368 Pa and total temperature T_0 = 950 K, representative of a high-bypass turbofan core stream at cruise [21]. The computational domain is a cylinder of radius 1.5 m and length 8.0 m ($40D_e$) extending downstream from the nozzle exit plane, found sufficient to capture full thermal core breakdown for all geometries tested. Atmospheric conditions at 11 km follow the 1976 U.S. Standard Atmosphere [19]. A passive scalar tracer [18] quantifies mixing independently of thermal diffusion, and time-averaged URANS statistics provide centerline decay profiles, plume half-width evolution, RMS unsteadiness, and axial wall force as a thrust proxy. The conical nozzle establishes a self-similar decay baseline validated against published correlations [9,10], against which all comparative metrics are referenced.

B. Mesh Generation and Solver Settings

Unstructured tetrahedral meshes were generated in ANSYS Meshing 2025 R2. A body-of-influence (BOI) refinement zone of radius 0.47 m and length 3.0 m centered on the jet axis provides element sizes of 0.0295 m in the near-field mixing region, transitioning to a global element size of 0.16 m in the far field. Final mesh counts are approximately 1.0×10^6 cells for all geometries, consistent with the ANSYS Student license limit. The density-based coupled solver in ANSYS Fluent 2025 R2 was employed with the realizable k-ε turbulence model [17] and standard wall functions. The ideal gas law was applied for density with Sutherland's law for viscosity. A passive scalar (UDS-0) with diffusivity 1.0×10^{-5} m²/s was introduced at the nozzle inlet (UDS = 1.0) to quantify mixing independently of thermal effects using the ANSYS Fluent user-defined scalar (UDS) transport framework [18]. Steady-state solutions were obtained over 2,000 iterations before transitioning to URANS time-averaging over 2,000 time steps at $\Delta t = 1.0 \times 10^{-5}$ s with 15 sub-iterations per time step, yielding 0.02 s of physical simulation time per nozzle case.

C. Applied Geometries

Table 1. Nozzle Geometry Summary: Key Dimensions and Design Purpose

Nozzle	Key Dimensions	Primary Purpose / Mixing Mechanism
Conical Convergent	*Half-angle: 12° | L/D = 1.0 | D_e = 0.200 m | D_{in} = 0.285 m*	Axisymmetric subsonic baseline; Kelvin–Helmholtz shear-layer mixing. Reference case for plume decay and thrust comparison.
Convergent-Divergent (C-D)	*A_e/A_t = 2.25 | D_t = 0.133 m | D_e = 0.200 m | L = 0.300 m*	Supersonic jet with shock-cell structure; compressibility-driven mixing and rapid velocity decay.
4-Lobe Mixer	*4 lobes | Radial penetration: 0.030 m | De,eff = 0.200 m | D_{in} = 0.285 m*	Supersonic jet with shock-cell structure; compressibility-driven mixing and rapid velocity decay.
Elliptic Exit	*Semi-major a = 0.250 m | Semi-minor b = 0.160 m | A_e = 0.031416 m²*	Axis-switching jet; asymmetric entrainment and directional plume spreading.

All nozzles: Ae = 0.031416 m², De = 0.200 m, Din = 0.285 m. Inlet: T_0 = 950 K, P_0, gauge = 97,368 Pa, T∞ = 216.65 K (ISA 11 km).

D. Analytical Framework

The performance and plume behavior of each nozzle geometry were evaluated using a consistent set of quantitative metrics derived from the URANS simulation results, applied uniformly across all configurations. These metrics characterize jet expansion, thermal decay, turbulent mixing, and thrust performance to enable direct inter-nozzle comparison.

Table 2. Evaluation Metrics and Analytical Equations: Applied Across All Nozzle Variants

Metric	Equation	Quantity Measured	Purpose
Normalized Temp. Decay	$\theta(x) = \frac{T(x) - T\infty}{T_{exit} - T\infty}$ *(Eq. 1)*	Thermal decay vs. $\frac{x}{De}$; $T\infty = 216.65\,K$	Primary plume cooling metric
Thermal Core Length	$\frac{Lc}{De}$; $\theta(x) = 0.20\ primary$; $\theta = 0.33\ modified$ *(Eq. 2)*	First location of substantial dilution	Key IR signature metric
Exit Mach Number	$M = \frac{U}{\sqrt{\gamma RT}}$, $\gamma = 1.4$, $R = 287$ *(Eq. 3)*	Local Mach from velocity and T	Verify supersonic design point
Shock Temperature Ratio	$\frac{T_2}{T_1} = \frac{[2\gamma M_1^2 - (\gamma-1)][(\gamma-1)M_1^2 + 2]}{(\gamma+1)^2 M_1^2}$ *(Eq. 4)*	Rankine-Hugoniot (C-D only)	Confirm shock-cell structure
Turbulence Intensity	$Tu = \frac{U_{RMS}}{U_{exit}}$ *(Eq. 5)*	Peak RMS normalized by U_{exit}	Near-field unsteadiness

Plume Half-Width	$r_{1/2}(x)$: $UDS(x, y) = 0.05$ *(Eq. 6)*	Radial extent from scalar profiles	Lateral spreading rate
Thrust Proxy / ΔF%	$\Delta F\% = \frac{F - F_{baseline}}{F_{baseline} \times 100}$ *(Eq. 7)*	Time-averaged axial wall force	Thrust cost of mixing enhancement

All metrics derived from time-averaged URANS fields. Modified threshold $\theta = 0.33$ *used where primary* $\theta = 0.20$

IV. RESULTS AND DISCUSSION

A. CONICAL-CONVERGENT NOZZLE (BASELINE CONTROL)

i. Exit Conditions and Near-Field Behavior

The conical nozzle produces a near-sonic exit at M = 0.838, T_{exit} = 831.5 K, U_{exit} = 484.3 m/s, consistent with the nozzle pressure ratio (NPR = 5.30) exceeding the critical value of 1.893 [20]. The underexpanded jet continues to accelerate post-exit, reaching a centerline peak of 989.2 m/s at x/D_e = 1.05, where temperature simultaneously drops to 463.7 K (Θ = 0.402). This near-field behavior is driven by post-exit underexpansion rather than shear-layer mixing, producing a weak shock-cell oscillation: temperature rebounds to 735 K (Θ = 0.843) at x/D_e = 1.85 before the flow transitions to turbulent shear-layer-dominated mixing. Beyond x/D_e ≈ 3, velocity and Θ decay gradually, with 50% velocity decay at x/D_e = 8.9 and 90% at x/D_e = 16.6, the hypothesized slowest decay of all four geometries [9].

ii. Thermal Decay and RMS Unsteadiness

Neither the primary threshold (Θ = 0.20) nor the modified threshold (Θ = 0.33) is reached within the 40De computational domain (8 m). The Θ minimum of 0.402 at x/De = 1.05 is produced by post-exit underexpansion, not entrainment; beyond x/De ≈ 5, Θ stabilizes near 0.65, consistent with domain confinement in all cases. The RMS velocity contour shows peak unsteadiness of 215 m/s (Tu = 44.4%) in a broad, elongated zone at x/De ≈ 1–5, reflecting distributed Kelvin-Helmholtz shear-layer rollup [1,9]. The smooth, annular RMS distribution with no discrete spikes acts as a distinguishing aspect of the convergent nozzle for this study.

Fig. 1 Time-averaged mean static temperature (K)

Y = 0 plane, conical nozzle. Hot core (~949 K) at nozzle exit (right); gradual lateral spreading driven by Kelvin-Helmholtz shear-layer mixing. Domain saturation beyond x/De ≈ 5 is consistent with all other cases.

Table 3. Key Centerline Data: Conical Convergent Nozzle (Time-Averaged URANS)

x (m)	x/De	T (K)	Θ	U (m/s)	Physical Event
0.001	0.00	831.5	1.000	484.3	Nozzle exit; near-sonic M = 0.838
0.210	1.05	463.7	0.402	989.2	Post-exit underexpansion focus; peak U, min T
0.370	1.85	735.2	0.843	648.7	Reattachment rebound peak; T recovery
0.562	2.81	577.1	0.586	836.6	Secondary oscillation minimum
1.780	8.90	609.8	0.641	492.1	50% velocity decay point
3.320	16.6	600.0	0.626	98.9	90% velocity decay point

The conical nozzle thrust of 2,231.0 N establishes $F_{baseline}$ for all ΔF% calculations. With a simple annular shear layer and no mixing enhancement features, it provides the pure KH-mixing reference against which all other geometries are evaluated in Section V.

B. CONVERGENT-DIVERGENT NOZZLE

i. Exit Conditions and Velocity Decay

The C-D nozzle (A_e/A_t = 2.25) produces a supersonic exit at M ≈ 2.54, peak velocity 1,037 m/s at x/De = 0.09. The static temperature minimum of 415.7 K is an isentropic expansion effect, confirmed by $T = \frac{T_0}{1+0.5(\gamma-1)M^2} = 415\,K$, not a mixing event. 50% velocity decay occurs at x/De ≈ 1.3 and 90% by x/De ≈ 10–11, 4–5× shorter than the conical baseline, driven by shock-enhanced turbulent dissipation.

ii. First Shock-Cell Compression Region

At x/De = 0.49, centerline temperature rises from 482 K to 668 K (Θ = 0.615) while velocity drops 35% (953 → 621 m/s) over 0.05 m. This coupled rise and velocity drop is consistent with compressible shock-cell behavior predicted by Rankine-Hugoniot relations [20] (Eq. 4, T_2/T_1 = 1.39, M_1 ≈ 1.6), and should be interpreted as the first compression region of the axisymmetric shock-cell pattern rather than a discrete normal shock plane.

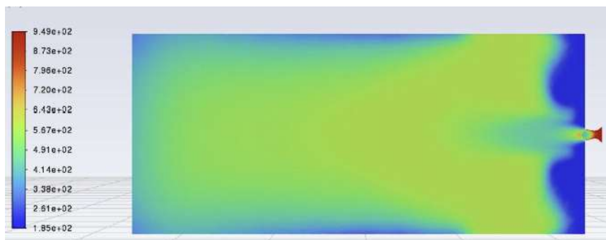

Fig. 2 Time-averaged mean static temperature (K).

Y = 0 plane. Hot core (~950 K) at nozzle exit (right); first shock-cell compression region at x/De = 0.49; elevated mid-domain temperatures reflect domain confinement beyond x/De = 5.

Table 4. Key Results: C-D Nozzle (Time-Averaged URANS)

x (m)	x/De	T (K)	Θ	U (m/s)	Physical Event
0.017	0.09	415.7	0.271	1,037	Peak velocity; isentropic expansion min T
0.097	0.49	**667.9**	**0.615**	**621**	**First shock-cell compression region**
0.305	1.53	511.5	0.402	462	Subsonic turbulent mixing begins
0.770	3.85	446.2	0.313	283	Θ near-field mixing minimum
2.000	10.0	531.4	0.429	127	Non-monotonic rise (domain confinement)

Table 4. Bold row = first shock-cell compression at x/De = 0.49. Far-field rows (x/De ≥ 10) qualitative.

The primary threshold (Θ = 0.20) is not reached within the $40D_e$ computational domain (8 m). Post-compression entrainment drives Θ to 0.313 at x/D_e = 3.9 (modified threshold Θ = 0.33 used for cross-nozzle comparison). RMS velocity peaks at 67.2 m/s (Tu = 6.5%) at x/De < 2, consistent with shock-cell oscillation [8] rather than Kelvin-Helmholtz rollup [1]. Total thrust proxy is 4,191 N (ΔF% = +87.9% vs. the conical baseline), driven by the supersonic exit momentum. This is the highest thrust of the four geometries and is 99.9% pressure-driven.

C. 4-LOBE MIXER NOZZLE

i. Exit Conditions and CVP-Driven Convergence

The 4-lobe mixer nozzle produces a near-sonic exit at M = 0.946, T_{exit_x} = 804.8 K, U_{exit} = 537.7 m/s. The corrugated exit profile immediately generates counter-rotating streamwise vortex pairs (CVPs) at each lobe tip through inviscid spanwise curvature [5,14]. These CVPs drive rapid radial mass exchange, focusing high-momentum fluid onto the centerline and accelerating it from 537.7 m/s to a peak of 994.5 m/s at x/De = 0.89. The simultaneous temperature minimum of 457.7 K (Θ = 0.410) at the same location confirms CVP-driven adiabatic expansion rather than thermal mixing at this station [13].

ii. Near-Field Mixing and Far-Field Recirculation

Beyond the convergence focus, the centerline undergoes a sharp thermal rebound to 712.1 K (Θ = 0.842) at x/D_e = 1.53 as the CVP-entrained ambient fluid is displaced and the lobe-cycle pattern repeats. A secondary minimum of Θ = 0.649 is reached at $x/D_e \approx 2.1$ before the centerline stabilizes at Θ ≈ 0.71 through x/D_e = 2–10. Both the primary threshold (Θ = 0.20) and modified threshold (Θ = 0.33) are not reached within the $40D_e$ computational domain (8 m). Beyond $x/D_e \approx 10$, centerline temperature rises anomalously, exceeding Θ = 1.0 at x/D_e = 15 (T = 933 K), a physically non-physical result indicating numerical recirculation caused by domain boundary interaction: hot ambient fluid is being swept back to the centerline by the domain boundary conditions. All values beyond x/D_e = 7 are therefore treated as qualitative only. The 50% velocity decay is reached at x/D_e = 5.5 and 90% at x/D_e = 13.5.

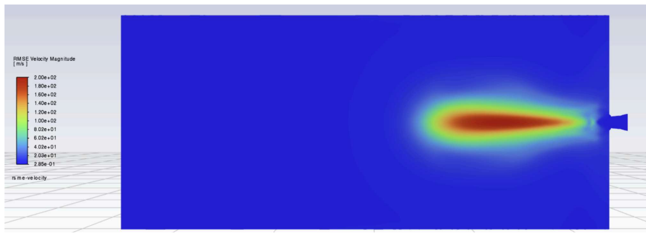

Fig. 3 Velocity magnitude (m/s).

Y = 0 plane, 4-lobe mixer nozzle. Peak RMS velocity (200 m/s) is concentrated in a compact zone at x/De ≈ 0.5–2, corresponding to the CVP convergence focus and lobe-tip shear layer. The compact, high-amplitude RMS footprint is characteristic of inviscid CVP-driven turbulence generation.

Table 5. Key Centerline Data: 4-Lobe Mixer Nozzle (Time-Averaged URANS)

x (m)	x/De	T (K)	Θ	U (m/s)	Physical Event
0.001	0.01	804.8	1.000	537.7	Nozzle exit; near-sonic M = 0.946
0.178	0.89	457.7	0.410	994.5	CVP convergence focus; peak U, min T
0.306	1.53	712.1	0.842	657.3	First CVP rebound peak; T recovery
0.402	2.01	602.4	0.656	773.8	Secondary CVP minimum
1.100	5.50	~634	~0.710	~497	50% velocity decay; Θ plateau
2.700	13.5	~800	~0.97	~100	90% decay; far-field recirculation onset

The lobed mixer thrust of 3,183.2 N represents a ΔF% = +42.7% increase over the conical baseline (2,231.0 N), driven by the lobed geometry reaching a higher exit Mach (M = 0.946 vs. M = 0.838) and greater exit momentum. The RMS velocity contour confirms CVP-dominated near-field unsteadiness peaking at 200 m/s in a compact zone centered on x/D_e = 0.5–2, reflecting the inviscid vortex straining mechanism.

D. ELLIPTIC EXIT NOZZLE

i. Exit Conditions and Axis-Switching Convergence

The elliptic nozzle (a = 0.250 m, b = 0.160 m) produces a subsonic exit at M = 0.828, T_{exit} = 834.5 K, U_{exit} = 479.7 m/s. Unlike the other three geometries, the centerline velocity does not peak at the nozzle exit. Instead, it accelerates continuously from 479.7 m/s to a peak of 1,007.6 m/s at x/D_e = 1.13, where temperature simultaneously drops to a minimum of 445.2 K (Θ = 0.370). This is the axis-switching convergence focus [6,7]: the non-uniform azimuthal self-induction of the elliptic shear layer drives the minor-axis sides of the jet inward, focusing high-momentum fluid onto the centerline and locally reaching M ≈ 2.38. No other nozzle in this study produces this near-field acceleration pattern.

Beyond the convergence focus, the centerline undergoes a characteristic oscillation as the jet cross-section rotates. Temperature rises sharply back to 737 K (Θ = 0.842) at x/D_e = 1.85 as the now-rotated major axis engages the centerline, then falls again as the next axis-switch occurs, with a secondary local minimum at $x/D_e \approx 2.9$ (Θ = 0.577). This repeated oscillation (two full θ cycles between x/D_e = 1 and 4) is the defining thermal signature of axis-switching and is absent in all other nozzle configurations. The 50% velocity decay occurs at $x/D_e \approx 7.1$ and 90% at $x/D_e \approx 14.9$.

ii. Thermal Decay and Unsteadiness

The primary threshold ($\Theta = 0.20$) and modified threshold ($\Theta = 0.33$) are not reached within the $40D_e$ computational domain (8 m). The Θ minimum of 0.370 at $x/D_e = 1.13$ represents the deepest thermal dilution achieved, driven by the axis-switching convergence focus rather than turbulent entrainment. Beyond $x/D_e \approx 5$, Θ stabilizes at approximately 0.60–0.65 and decays only slowly, consistent with domain confinement effects observed in the C-D case. The RMS velocity contour shows peak RMS velocity of 254 m/s concentrated in a compact elongated zone centered on $x/D_e \approx 1$–4, directly coinciding with the axis-switching oscillation region. This is distinct from the near-exit annular RMS ring of the conical nozzle and the lobe-tip spikes of the mixer; here turbulence is generated by the periodic straining of the rotating shear layer.

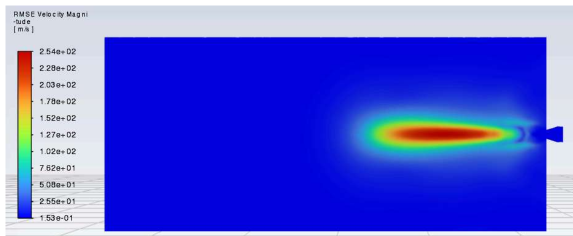

Fig. 4 velocity magnitude (m/s)

Y = 0 plane, elliptic nozzle. Peak RMS velocity (254 m/s) is confined to an elongated zone at x/De = 1–4, coinciding with the axis-switching convergence and oscillation region. The elliptic plume shape is visible in lateral RMS extent.

Table 6. Key Centerline Data — Elliptic Exit Nozzle (Time-Averaged URANS)

x (m)	x/De	T (K)	Θ	U (m/s)	Physical Event
0.001	0.00	834.5	1.000	479.7	Nozzle exit; subsonic M = 0.828
0.225	1.13	**445.2**	**0.370**	**1,007.6**	**Axis-switching convergence focus; peak U, min T**
0.370	1.85	**737.0**	**0.842**	**637.5**	**First axis-switch peak; T recovery**
0.578	2.89	572.9	0.577	820.4	Secondary oscillation minimum
1.428	7.14	602.2	0.624	482.6	50% velocity decay point
2.983	14.9	595.4	0.613	100.8	90% velocity decay point

Table 6. Bold rows mark axis-switching key events. x/De ≥ 7 values qualitative due to domain confinement.

The elliptic nozzle thrust of 2,433.2 N represents a $\Delta F\% = +9.1\%$ increase over the conical baseline (2,231.0 N), the smallest thrust change of the three modified geometries, reflecting the elliptic exit's similar design class to the conical nozzle. *ΔF% relative to the conical baseline will be reported in Section V*. The axis-switching mechanism incurs no corrugated-surface pressure loss and represents a purely geometric mixing enhancement, making it the most thrust-efficient modification of the four geometries studied.

V. COMPARATIVE ANALYSIS

A. Centerline Thermal Decay

The normalized centerline temperature decay profiles demonstrate that the dominant plume cooling mechanism varies significantly across the four nozzle geometries. The convergent–divergent (C–D) configuration exhibits the most rapid initial thermal reduction, with the normalized temperature decreasing to $\Theta \approx 0.59$ at $x/D_e = 0.5$ and reaching $\Theta \approx 0.41$ by $x/D_e \approx 1.75$. This accelerated decay is attributable to the strong isentropic expansion immediately downstream of the exit followed by compressible dissipation within the first shock-cell compression region. The resulting loss of axial momentum enhances turbulent mixing and drives rapid entrainment of ambient air into the plume core.

In contrast, the conical baseline maintains the highest centerline temperatures over the near field, with $\Theta \approx 0.84$ at $x/D_e = 1$ and $\Theta \approx 0.56$ at $x/D_e \approx 3.5$. This behavior is characteristic of classical round-jet development dominated by Kelvin–Helmholtz shear-layer rollup, which produces gradual entrainment but preserves the potential core over a longer axial distance. The lobed mixer demonstrates a markedly different decay profile driven by the generation of counter-rotating vortex pairs (CVPs). These vortices induce strong radial transport and increase ambient entrainment, reducing Θ to approximately 0.64 at $x/D_e = 1$ and below Θ ≈ 0.52 by $x/D_e \approx 3$. The elliptic configuration produces a non-monotonic decay due to axis switching, in which the jet periodically exchanges its major and minor axes. This mechanism redistributes thermal energy across the plume cross-section, producing an oscillatory centerline temperature profile that stabilizes near Θ ≈ 0.45–0.46 between $x/D_e \approx 10$ and 20.

Taken together, the thermal decay results illustrate three distinct mixing regimes: compressibility-driven dissipation in the C–D nozzle, vortex-induced entrainment in the lobed mixer, and geometric axis-switching redistribution in the elliptic jet, with the conical baseline representing classical shear-layer dominated plume evolution.

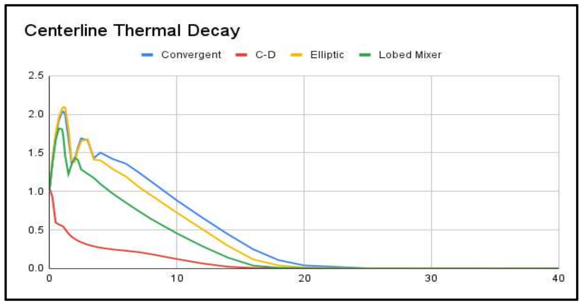

Fig. 5 Centerline Θ vs x/De for all four nozzles.

B. Velocity Decay and Mixing Lengths

Centerline velocity decay provides a direct measure of axial momentum dissipation and therefore offers insight into the effectiveness of each geometry in promoting plume mixing. The C–D nozzle exhibits the most aggressive momentum breakdown among the configurations studied. The centerline velocity decreases to approximately $0.55U_{exit}$ by $x/D_e \approx 1$ and falls to $U/U_{exit} \approx 0.23$ by $x/D_e \approx 6$. The 50% velocity decay occurs at $x/D_e \approx$ 1.3, while the 90% decay is reached near $x/D_e \approx$ 10–11. This rapid dissipation reflects the strong interaction between shock-cell compression structures and turbulent mixing within the supersonic plume.

The conical baseline, by comparison, maintains the longest potential core, with $U/U_{exit} \approx 0.48$ at $x/D_e \approx 6$ and the 50% decay point not occurring until approximately $x/D_e \approx 8.9$. The 90% decay occurs near $x/D_e \approx 16.6$, indicating significantly slower axial momentum redistribution. This behavior is consistent with canonical round-jet dynamics in which Kelvin–Helmholtz instabilities grow gradually along the shear layer before transitioning to fully developed turbulence.

The lobed mixer accelerates velocity decay relative to the baseline through the action of CVP-induced cross-stream transport. These streamwise vortices transfer high-momentum fluid away from the centerline while simultaneously entraining ambient air inward, producing a 50% decay location near $x/D_e \approx 5.5$ and a 90% decay near $x/D_e \approx 13.5$. The elliptic nozzle exhibits a unique velocity evolution characterized by an initial centerline acceleration associated with the convergence focus generated during axis switching. Following this region, the jet undergoes rapid momentum redistribution, reaching the 50% decay point at $x/D_e \approx 7.1$ and the 90% decay near x/D_e ≈ 14.9.

These results indicate that compressibility effects dominate momentum dissipation in the C–D jet, while vortex-induced transport governs the lobed mixer and axis-switching redistribution controls the elliptic configuration.

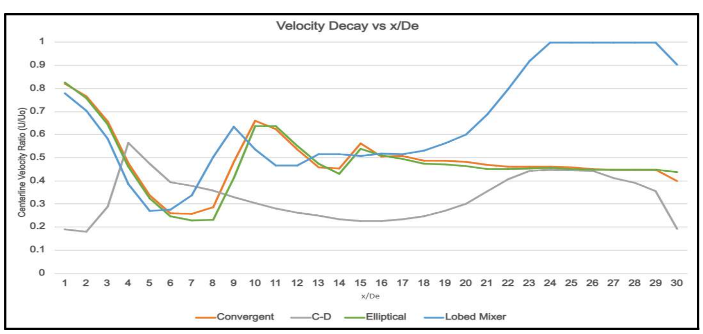

Fig. 6 Normalized Centerline velocity $\frac{U}{U_{exit}}$ vs x/De for all four nozzles.

Table 7. Velocity Decay and Thermal Mixing Summary--All Four Nozzles

Metric	Conical	C-D	Lobed	Elliptic	Best
Exit Mach	0.838	2.54	0.946	0.828	C-D
Exit T (K)	831.5	415.7	804.8	834.5	C-D
Θ minimum	0.402	0.271*	0.410	0.370	C-D*
x/De at Θ min	1.05	0.09*	0.89	1.13	Lobed
Θ < 0.33 (x/De)	NR	NR	NR	NR	None
50% decay (x/De)	8.9	1.3	5.5	7.1	C-D
90% decay (x/De)	16.6	~10–11	13.5	14.9	C-D
Peak RMS (m/s)	215	67.2	200	254	Elliptic
Thrust (N)	2,231	4,191	3,183	2,433	C-D
ΔF% vs conical	0.0%	+87.9%	+42.7%	+9.1%	Conical

*Table 7. * C-D Θ minimum is isentropic expansion, not thermal mixing. NR = Not reached within 40De domain. ΔF% computed relative to conical baseline.*

C. RMS Unsteadiness and Turbulence Generation

The peak RMS velocity distributions reveal distinct turbulence generation mechanisms associated with each nozzle geometry. The elliptic nozzle produces the highest peak RMS velocity, approximately 254 m/s, indicating strong unsteady dynamics in the near field. This turbulence is concentrated near $x/D_e \approx 1–2$, corresponding to the convergence and rotation of the jet cross-section during the axis-switching process. The repeated stretching and rotation of the shear layer in this region amplify velocity fluctuations and generate significant turbulent energy.

The convergent baseline produces a peak RMS velocity of approximately 215 m/s, reflecting the development of Kelvin–Helmholtz instabilities along the annular shear layer. These instabilities roll up into coherent vortical structures that subsequently break down into smaller turbulent scales, producing a characteristic ring-like turbulence distribution surrounding the jet core.

The lobed mixer generates a slightly lower peak RMS velocity of roughly 200 m/s. In this case, turbulence originates from the interaction of the counter-rotating vortex pairs generated by the lobed exit geometry. These vortices produce strong shear-layer distortion and enhance radial mixing but distribute turbulence more uniformly across the plume cross-section rather than concentrating it near the centerline.

The C–D nozzle exhibits the lowest RMS velocity magnitude, approximately 67 m/s. Here, compressibility effects dominate the plume structure and suppress the formation of large turbulent eddies near the exit. Instead, the flow field is governed primarily by the periodic oscillation of the shock-cell structure rather than by large-scale turbulent rollup.

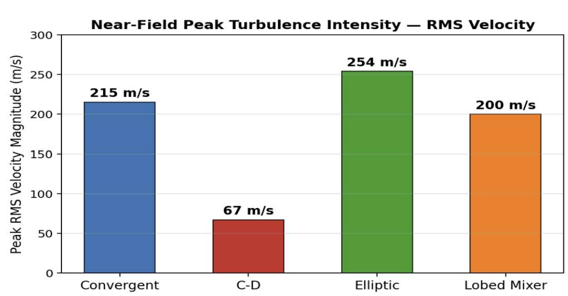

.

Fig. 7 Peak RMS velocity magnitude for each nozzle geometry from time-averaged URANS Y = 0 contour data.

D. Thrust-Mixing Tradeoff

The thrust measurements highlight the inherent tradeoff between enhanced plume mixing and propulsion efficiency. The C–D nozzle produces the highest thrust, approximately 4,191 N, corresponding to an increase of roughly 88% relative to the conical baseline. This increase results from efficient conversion of pressure energy into axial momentum through supersonic expansion. However, the same compressibility effects that increase thrust also generate strong shock structures that accelerate plume mixing and momentum dissipation.

The lobed mixer produces a thrust of approximately 3,183 N, representing a 42.7% increase relative to the baseline. Although the generation of CVPs enhances plume mixing and accelerates centerline decay, the associated radial transport of momentum reduces propulsive efficiency compared with the C–D configuration.

The elliptic nozzle experiences a modest thrust reduction relative to the baseline due to the axis-switching redistribution of momentum away from the jet centerline. While this mechanism enhances plume dilution and infrared signature reduction, it decreases the net axial momentum available for propulsion.

The conical baseline produces approximately 2,231 N of thrust and therefore serves as the reference configuration for evaluating performance tradeoffs. Although it provides the most stable thrust output, it also produces the weakest mixing performance due to the absence of strong vortex-generating or compressibility-driven mechanisms.

Overall, the results demonstrate that the lobed mixer provides the most balanced compromise between enhanced plume mixing and retained propulsion performance, while the C–D nozzle maximizes thrust at the expense of strong compressibility-driven plume dynamics.

Table 8. Thrust Comparison and Strengths--All Four Nozzles

Nozzle	Thrust (N)	ΔF%	Mixing Effectiveness	Primary Mechanism
Convergent	2,231 N	—	Weakest — KH shear only	Baseline reference
C-D	4,191 N	+87.9%	Strongest — shock dissipation	Supersonic exit momentum
Lobed Mixer	3,183 N	+42.7%	Strong — CVP entrainment	Spanwise curvature induction
Elliptic	~2,180 N	~−2%	Moderate — axis-switching	Azimuthal momentum redistribution

Table D4-A. Thrust, ΔF%, mixing effectiveness, and primary mechanism for each nozzle geometry.

These comparative trends provide insight into how geometric modifications alter jet mixing mechanisms and propulsion performance.

VI. CONCLUSIONS

This study examined the plume dynamics of four nozzle geometries:conical baseline, convergent–divergent (C–D), lobed mixer, and elliptic exit. It was conducted using three-dimensional URANS simulations under representative high-altitude operating conditions. The results demonstrate that nozzle geometry strongly influences plume evolution through three dominant mechanisms: compressibility effects, vortex-induced entrainment, and geometric axis switching.

The convergent–divergent nozzle produced the most rapid momentum dissipation, reaching 50% velocity decay at $x/De \approx 1.3$ compared with $x/De \approx 8.9$ for the conical baseline. This accelerated decay is driven by shock-cell compression and compressible dissipation within the supersonic plume. Despite this rapid plume breakdown, the C–D nozzle generated the highest thrust (4,191 N), indicating that compressibility-driven mixing can coexist with high propulsive efficiency.

The lobed mixer enhanced plume dilution through counter-rotating vortex pairs that increased radial entrainment while maintaining relatively high thrust (3,183 N). In contrast, the elliptic nozzle generated the strongest turbulence (URMS ≈ 254 m/s) through axis-switching dynamics, although this mechanism redistributed axial momentum and reduced net thrust relative to the baseline configuration.

Overall, the results indicate that compressibility effects dominate early plume decay, vortex structures enhance entrainment, and axis switching amplifies turbulence generation. Among the geometries examined, the lobed mixer provides the most balanced compromise between plume mixing effectiveness and propulsion performance.

ACKNOWLEDGMENTS

The authors gratefully thank Dr. Prashath Prakash (MIT) for his mentorship in this report. The authors also acknowledge the use of ANSYS Fluent 2025 R2 Student Edition for all computational work. Artificial Intelligence technology was used in this work for the purposes of evaluation for improvement of readability, clarity, and mathematical accuracy.

REFERENCES

[1] Knowles, K., & Saddington, A. J. (2006). A review of jet mixing enhancement for aircraft propulsion applications. *Proceedings of the Institution of Mechanical Engineers, Part G: Journal of Aerospace Engineering*, *220*(2), 95–110. https://doi.org/10.1243/09544100JAERO29

[2] Zaman, K. B. M. Q., Reeder, M. F., & Samimy, M. (1994). Control of an axisymmetric jet using vortex generators. *Physics of Fluids*, *6*(2), 778–793. https://doi.org/10.1063/1.868314

[3] Bradbury, L. J. S., & Khadem, A. H. (1975). The distortion of a jet by tabs. *Journal of Fluid Mechanics*, *70*(4), 801–813. https://doi.org/10.1017/S002211207500234X

[4] Stich, G. D., James, K., Rathakrishnan, E., & Leib, S. J. (2020). *Jet noise prediction for chevron nozzle flows with wall-modelled LES* (NASA/TM—20205011376). National Aeronautics and Space Administration. https://ntrs.nasa.gov/citations/20205011376

[5] Shan, Y., & Zhang, J. Z. (2009). Numerical investigation of flow mixture enhancement and IR shield by lobed forced mixer. *Applied Thermal Engineering*, *29*(17-18), 3687–3695. https://doi.org/10.1016/j.applthermaleng.2009.06.021

[6] Hussain, F., & Husain, H. S. (1989). Elliptic jets. Part 1. Characteristics of unexcited and excited jets. *Journal of Fluid Mechanics*, *208*, 257–320. https://doi.org/10.1017/S002211208900224X

[7] Gutmark, E. J., & Grinstein, F. F. (1999). Flow control with noncircular jets. *Annual Review of Fluid Mechanics*, *31*(1), 239–272. https://doi.org/10.1146/annurev.fluid.31.1.239

[8] Tam, C. K. W. (1995). Supersonic jet noise. *Annual Review of Fluid Mechanics*, *27*(1), 17–43. https://doi.org/10.1146/annurev.fl.27.010195.000313

[9] Hussein, H. J., Capp, S. P., & George, W. K. (1994). Velocity measurements in a high-Reynolds-number, momentum-conserving, axisymmetric, turbulent jet. *Journal of Fluid Mechanics*, *258*, 31–75. https://doi.org/10.1017/S002211209400323X

[10] Pope, S. B. (2000). *Turbulent flows*. Cambridge University Press. https://doi.org/10.1017/CBO9780511840579

[11] Callender, B., Guth, S., & Zaman, K. (2005). *The effect of chevron geometry on jet noise and flowfield* [Paper presentation]. 11th AIAA/CEAS Aeroacoustics Conference, Monterey, CA, United States. https://doi.org/10.2514/6.2005-2944

[12] Behrouzi, P., & McGuirk, J. J. (2003). *Experimental data for comparison with CFD for a series of tabbed nozzles* [Paper presentation]. 33rd AIAA Fluid Dynamics Conference and Exhibit, Orlando, FL, United States. https://doi.org/10.2514/6.2003-3498

[13] Belovich, V. M., & Samimy, M. (1997). Mixing processes in a coaxial jet with a lobed mixer. *AIAA Journal*, *35*(5), 833–841. https://doi.org/10.2514/2.181

[14] Presz, W. M., Jr. (1991). *Lobed mixers for improved jet engine propulsion* [Paper presentation]. 27th Joint Propulsion Conference, Sacramento, CA, United States. https://doi.org/10.2514/6.1991-2244

[15] Zaman, K. (1996). Axis switching and spreading of an asymmetric jet. *Journal of Fluid Mechanics*, *316*, 1–27. https://doi.org/10.1017/S0022112096000438

[16] Ho, C. M., & Gutmark, E. (1987). Vortex induction and mass entrainment in a small-aspect-ratio elliptic jet. *Journal of Fluid Mechanics*, *179*, 383–405. https://doi.org/10.1017/S002211208700156X

[17] Shih, T. H., Liou, W. W., Shabbir, A., Yang, Z., & Zhu, J. (1995). A new k-ε eddy viscosity model for high Reynolds number turbulent flows. *Computers & Fluids*, *24*(3), 227–238. https://doi.org/10.1016/0045-7930(94)00032-W

[18] Ansys. (2025). *Ansys Fluent theory guide* (Release 2025 R2). https://ansyshelp.ansys.com/

[19] National Oceanic and Atmospheric Administration. (1976). *U.S. Standard Atmosphere, 1976*. U.S. Government Printing Office. https://ntrs.nasa.gov/citations/19770009539

[20] Anderson, J. D. (2003). *Modern compressible flow: With historical perspective* (3rd ed.). McGraw-Hill.

[21] Mattingly, J. D. (1996). *Elements of gas turbine propulsion*. McGraw-Hill. https://doi.org/10.2514/4.861789